

MULTISPHALERONS IN THE WEINBERG-SALAM THEORY

Burkhard Kleihaus

Fachbereich Physik, Universität Oldenburg, Postfach 2503
D-26111 Oldenburg, Germany

Jutta Kunz

Fachbereich Physik, Universität Oldenburg, Postfach 2503
D-26111 Oldenburg, Germany

and

Instituut voor Theoretische Fysica, Rijksuniversiteit te Utrecht
NL-3508 TA Utrecht, The Netherlands

May 26, 1994

Abstract

We construct multisphaleron solutions in the Weinberg-Salam theory. The multisphaleron solutions carry Chern-Simons charge $n/2$, where n is an integer, counting the winding of the fields in the azimuthal angle. The well-known sphaleron has $n = 1$. The multisphalerons possess axial symmetry and parity reflection symmetry. We vary the Higgs mass and the mixing angle. For small n the energies of the multisphalerons are on the order of n times the energy of the sphaleron and their magnetic dipole moments are on the order of n times the magnetic dipole moment of the sphaleron.

1 Introduction

In 1976 't Hooft [1] observed that the standard model does not absolutely conserve baryon and lepton number due to the Adler-Bell-Jackiw anomaly. In particular 't Hooft considered spontaneous fermion number violation due to instanton transitions between topologically inequivalent vacua. Recently fermion number violating tunnelling transitions at high energies attracted much attention [2, 3].

In 1983 Manton [4] reconsidered the possibility of fermion number violation in the electroweak theory. By constructing a non-contractible loop in the configuration space of the Weinberg-Salam theory Manton predicted the existence of a static, unstable solution of the field equations, a sphaleron [5], representing the top of the energy barrier between topologically distinct vacua.

The sphaleron is relevant in cosmology for the baryon asymmetry of the universe. At finite temperature the energy barrier between distinct vacua can be overcome due to thermal fluctuations of the fields, and vacuum to vacuum transitions can occur, accompanied by a change of baryon and lepton number. The rate for such baryon number violating processes is largely determined by a Boltzmann factor, containing the height of the barrier at a given temperature, and thus by the energy of the sphaleron [6, 7, 8, 9, 10].

The non-contractible loop constructed by Manton [4] corresponds to a non-trivial mapping $S_3 \rightarrow S_3$ with winding number one. Since $\pi_3(S_3) = \mathbb{Z}$, there exist non-contractible loops with higher winding numbers. While the minimal maximal energy configuration along the loops with winding number one corresponds to the sphaleron, there should be analogous extremal configurations for the loops with higher winding numbers. Correspondingly there should exist further unstable solutions of the Weinberg-Salam theory, multisphalerons [11].

In this paper we investigate the configuration space of the Weinberg-Salam theory further and construct multisphaleron solutions [11]. In contrast to the sphaleron [5] which is spherically symmetric for zero mixing angle, the multisphaleron solutions are only axially symmetric, even for zero mixing angle [11]. The appropriate ansatz for the multisphalerons represents a generalization of the axially symmetric ansatz for the sphaleron at finite mixing angle [11, 12, 13], preserving the invariance under parity.

The ansatz for the multisphalerons contains an integer n , representing the winding number with respect to the azimuthal angle ϕ . While ϕ covers the full trigonometric circle once, the fields wind n times around. The ansatz is thus analogous to the ansatz of Manton [14] and Rebbi and Rossi [15] for multimonopole solutions of an $SU(2)$ gauge theory with a Higgs triplet. The winding number n also determines the Chern-Simons charge of the multisphaleron solutions, $N_{\text{CS}} = n/2$, and thus also their baryon number [11].

In section 2 we briefly review the Weinberg-Salam lagrangian, discuss the ansatz

and present the resulting energy functional. We then point out a residual $U(1)$ gauge invariance of the energy functional. After fixing the gauge we specify the boundary condition for the fields. We present the Chern-Simons charge of the multisphaleron solutions, subject to these boundary conditions, and we consider the extraction of their electromagnetic properties. In section 3 we discuss the numerical procedure for solving the seven coupled non-linear partial differential equations. We then present the numerical results for the multisphaleron solutions with $n \leq 5$ for various values of the Higgs mass. While the multisphalerons were briefly described in [11] for zero mixing angle, we here consider the full range of the mixing angle, $0 \leq \theta_w \leq \pi/2$. We present our conclusions in section 4.

2 Ansatz and energy density

Let us consider the bosonic sector of the Weinberg-Salam theory

$$\mathcal{L} = -\frac{1}{4}F_{\mu\nu}^a F^{\mu\nu,a} - \frac{1}{4}f_{\mu\nu}f^{\mu\nu} + (D_\mu\Phi)^\dagger(D^\mu\Phi) - \lambda(\Phi^\dagger\Phi - \frac{v^2}{2})^2 \quad (1)$$

with the $SU(2)_L$ field strength tensor

$$F_{\mu\nu}^a = \partial_\mu V_\nu^a - \partial_\nu V_\mu^a + g\epsilon^{abc}V_\mu^b V_\nu^c, \quad (2)$$

with the $U(1)$ field strength tensor

$$f_{\mu\nu} = \partial_\mu A_\nu - \partial_\nu A_\mu, \quad (3)$$

and the covariant derivative for the Higgs field

$$D_\mu\Phi = \left(\partial_\mu - \frac{i}{2}g\tau^a V_\mu^a - \frac{i}{2}g'A_\mu\right)\Phi. \quad (4)$$

The gauge symmetry is spontaneously broken due to the non-vanishing vacuum expectation value v of the Higgs field

$$\langle\Phi\rangle = \frac{v}{\sqrt{2}} \begin{pmatrix} 0 \\ 1 \end{pmatrix}, \quad (5)$$

leading to the boson masses

$$M_W = \frac{1}{2}gv, \quad M_Z = \frac{1}{2}\sqrt{(g^2 + g'^2)}v, \quad M_H = v\sqrt{2\lambda}. \quad (6)$$

The mixing angle θ_w is determined by the relation $\tan\theta_w = g'/g$, and the electric charge is $e = g \sin\theta_w$.

Gauge field configurations can be classified by a charge, the Chern-Simons charge. The Chern-Simons current is not conserved, its divergence represents the U(1) anomaly of the baryon current. The SU(2) Chern-Simons current is given by

$$K_\mu = \frac{g^2}{16\pi^2} \varepsilon_{\mu\nu\rho\sigma} \text{Tr}(\mathcal{F}^{\nu\rho} \mathcal{V}^\sigma + \frac{2}{3}ig\mathcal{V}^\nu \mathcal{V}^\rho \mathcal{V}^\sigma) , \quad (7)$$

where $\mathcal{F}_{\nu\rho} = 1/2\tau^i F_{\nu\rho}^i$, and $\mathcal{V}_\sigma = 1/2\tau^i V_\sigma^i$, and the SU(2) Chern-Simons charge of a configuration is given by

$$N_{\text{CS}} = \int d^3r K^0 . \quad (8)$$

For the vacua the Chern-Simons charge is identical to the integer winding number, while the sphaleron has a Chern-Simons charge of 1/2 [5].

2.1 Ansatz

Let us now consider the ansatz for the multisphaleron solutions. Following Manton [14] and Rebbi and Rossi [15] we define a set of orthonormal vectors

$$\begin{aligned} \vec{u}_1^{(n)}(\phi) &= (\cos n\phi, \sin n\phi, 0) , \\ \vec{u}_2^{(n)}(\phi) &= (0, 0, 1) , \\ \vec{u}_3^{(n)}(\phi) &= (\sin n\phi, -\cos n\phi, 0) , \end{aligned} \quad (9)$$

and expand the fields as follows

$$V_i^a(\vec{r}) = u_j^{i(1)}(\phi) u_k^{a(n)}(\phi) w_j^k(\rho, z) , \quad (10)$$

$$A_i(\vec{r}) = u_j^{i(1)}(\phi) a_j(\rho, z) , \quad (11)$$

$$\Phi(\vec{r}) = i\tau^i u_j^{i(n)}(\phi) h_j(\rho, z) \frac{v}{\sqrt{2}} \begin{pmatrix} 0 \\ 1 \end{pmatrix} . \quad (12)$$

This ansatz has axial symmetry, i. e. a rotation about the z -axis can be compensated by a suitable gauge transformation [11, 12, 13]. To restrict the ansatz further we require invariance under the discrete transformation consisting of charge conjugation and reflection through the xz -plane (mirror symmetry). This leads to the conditions [11, 12, 13]

$$w_1^1(\rho, z) = w_2^1(\rho, z) = w_1^2(\rho, z) = w_2^2(\rho, z) = w_3^3(\rho, z) = 0 , \quad (13)$$

$$a_1(\rho, z) = a_2(\rho, z) = 0 , \quad (14)$$

$$h_3(\rho, z) = 0 . \quad (15)$$

2.2 Energy density

The resulting energy functional

$$E = \frac{1}{2} \int (E_w + E_a + v^2 E_h) d\phi \rho d\rho dz \quad (16)$$

then has the axially symmetric contributions

$$\begin{aligned} E_w &= (\partial_\rho w_3^1 + \frac{1}{\rho}(nw_1^3 + w_3^1) - gw_1^3 w_3^2)^2 + (\partial_z w_3^1 + \frac{n}{\rho}w_2^3 - gw_2^3 w_3^2)^2 \\ &+ (\partial_\rho w_3^2 + \frac{1}{\rho}w_3^2 + gw_1^3 w_3^1)^2 + (\partial_z w_3^2 + gw_2^3 w_3^1)^2 + (\partial_\rho w_2^3 - \partial_z w_1^3)^2, \end{aligned} \quad (17)$$

$$E_a = (\partial_\rho a_3 + \frac{1}{\rho}a_3)^2 + (\partial_z a_3)^2, \quad (18)$$

$$\begin{aligned} E_h &= (\partial_\rho h_1 - \frac{g}{2}w_1^3 h_2)^2 + (\partial_z h_1 - \frac{g}{2}w_2^3 h_2)^2 + (\partial_\rho h_2 + \frac{g}{2}w_1^3 h_1)^2 + (\partial_z h_2 + \frac{g}{2}w_2^3 h_1)^2 \\ &+ (\frac{n}{\rho}h_1 + \frac{g}{2}(w_3^1 h_2 - w_3^2 h_1) - \frac{g'}{2}a_3 h_1)^2 + (\frac{g}{2}(w_3^1 h_1 + w_3^2 h_2) - \frac{g'}{2}a_3 h_2)^2 \\ &+ \frac{\lambda v^2}{2}(h_1^2 + h_2^2 - 1)^2. \end{aligned} \quad (19)$$

2.3 Residual gauge invariance

The energy functional is still invariant under gauge transformations generated by

$$U = e^{i\Gamma(\rho, z)\tau^i u_3^{i(n)}} \quad (20)$$

analogous to [11, 12, 13, 14, 15]. Note, that under this transformation the 2-D Higgs doublets (h_1, h_2) and $(w_3^1, w_3^2 - n/g\rho)$ transform with angle $\Gamma(\rho, z)$ and $2\Gamma(\rho, z)$, respectively, while the 2-D gauge field (w_1^3, w_2^3) transforms inhomogeneously.

Here we fix this gauge degree of freedom by choosing the ‘Coulomb gauge’ condition [11, 12, 13]

$$\partial_\rho w_1^3 + \partial_z w_2^3 = 0. \quad (21)$$

This choice of gauge leads to regular solutions, while other choices of gauge are known to lead to singular solutions [13, 16].

2.4 Parity

In addition to axial, charge conjugation and mirror symmetry we also require parity reflection symmetry. Changing to spherical coordinates and extracting the trivial θ -dependence we specify the ansatz further [11, 12, 13]

$$\begin{aligned} w_1^3(r, \theta) &= \frac{2}{gr} F_1(r, \theta) \cos \theta, & w_2^3(r, \theta) &= -\frac{2}{gr} F_2(r, \theta) \sin \theta, \\ w_3^1(r, \theta) &= -\frac{2n}{gr} F_3(r, \theta) \cos \theta, & w_3^2(r, \theta) &= \frac{2n}{gr} F_4(r, \theta) \sin \theta, \end{aligned} \quad (22)$$

$$a_3(r, \theta) = \frac{2}{g'r} F_7(r, \theta) \sin \theta, \quad (23)$$

$$h_1(r, \theta) = F_5(r, \theta) \sin \theta, \quad h_2(r, \theta) = F_6(r, \theta) \cos \theta. \quad (24)$$

Note, that the spherically symmetric ansatz for the sphaleron corresponds to $n = 1$ and $F_1(r, \theta) = F_2(r, \theta) = F_3(r, \theta) = F_4(r, \theta) = f(r)$, $F_5(r, \theta) = F_6(r, \theta) = h(r)$, and $F_7(r, \theta) = 0$ (where the functions $f(r)$ and $h(r)$ correspond to those of Ref. [5]).

2.5 Boundary conditions

The above ansatz, when inserted into the classical equations of motion in the chosen gauge, yields a set of coupled partial differential equations for the functions $F_i(r, \theta)$, to be solved numerically subject to certain boundary conditions. To obtain regular, finite energy solutions with the imposed symmetries, we take as boundary conditions for the functions $F_i(r, \theta)$

$$\begin{aligned} r = 0 &: F_i(r, \theta)|_{r=0} = 0, \quad i = 1, \dots, 7, \\ r \rightarrow \infty &: F_i(r, \theta)|_{r=\infty} = 1, \quad i = 1, \dots, 6, \quad F_7(r, \theta)|_{r=\infty} = 0, \\ \theta = 0 &: \partial_\theta F_i(r, \theta)|_{\theta=0} = 0, \quad i = 1, \dots, 7, \\ \theta = \pi/2 &: \partial_\theta F_i(r, \theta)|_{\theta=\pi/2} = 0, \quad i = 1, \dots, 7. \end{aligned} \quad (25)$$

2.6 Chern-Simons charge

The Chern-Simons charge of the multisphaleron solutions can be evaluated analogously to the Chern-Simons charge of the sphaleron [5]. At spatial infinity the SU(2) vector fields are pure gauge configurations

$$\tau^a V_i^a = -\frac{2i}{g} \partial_i U(\infty) U^\dagger(\infty) \quad (26)$$

with

$$U(\infty) = i(\sin \theta \tau^i u_1^{i(n)} + \cos \theta \tau^i u_2^{i(n)}) . \quad (27)$$

The proper gauge for evaluating the Chern-Simons charge is the gauge with $U = 1$ at infinity, which is obtained with the transformation $U^\dagger(\vec{r})$

$$U(\vec{r}) = \exp\left(i\Omega(r, \theta)(\sin \theta \tau^i u_1^{i(n)} + \cos \theta \tau^i u_2^{i(n)})\right) \quad (28)$$

and the boundary conditions $\Omega(0) = 0$ and $\Omega(\infty) = \pi/2$ [5]. The SU(2) Chern-Simons charge of the multisphaleron solutions is then given by

$$N_{\text{CS}} = \frac{1}{2\pi^2} \int d^3r Q(\rho, z) , \quad (29)$$

where the SU(2) Chern-Simons density is determined by [17]

$$\begin{aligned} Q(\rho, z) &= n \frac{\sin^2 \Omega}{r^2} \frac{\partial \Omega}{\partial r} \\ &+ n \frac{\partial}{\partial z} \left(\frac{z}{4r^3} F_1 \sin(2\Omega) \right) + n \frac{\partial}{\rho \partial \rho} \left(\frac{\rho^2}{4r^3} F_2 \sin(2\Omega) \right) \\ &+ \frac{\cos^2 \theta}{4r^2} \frac{\partial}{\partial r} \left(F_3 \sin(2\Omega) \right) + \frac{\sin^2 \theta}{4r^2} \frac{\partial}{\partial r} \left(F_4 \sin(2\Omega) \right) \\ &+ \frac{1}{2\rho} \frac{\partial}{\partial z} \left(\frac{z\rho^2}{r^3} (F_3 - F_4) \frac{\partial \Omega}{\partial \rho} \right) - \frac{1}{2\rho} \frac{\partial}{\partial \rho} \left(\frac{z\rho^2}{r^3} (F_3 - F_4) \frac{\partial \Omega}{\partial z} \right) . \end{aligned} \quad (30)$$

Eq. (30) explicitly demonstrates the effect of a gauge transformation of the form (28). Only the first term of $Q(\rho, z)$ determines the SU(2) Chern-Simons charge, since the derivative terms do not contribute, due to the boundary conditions for the functions $F_i(r, \theta)$ and for $\Omega(r, \theta)$.

Since the U(1) field does not contribute to the Chern-Simons charge [5], the full Chern-Simons charge is given by the SU(2) Chern-Simons charge. We thus obtain for the multisphalerons the Chern-Simons charge

$$N_{\text{CS}} = n/2 , \quad (31)$$

independently of the Higgs mass and of the mixing angle, reproducing the well-known Chern-Simons charge of the sphaleron, $N_{\text{CS}} = 1/2$. The Chern-Simons charge of the sphaleron and of the multisphalerons corresponds to their baryonic charge, $Q_B = n/2$ [5].

2.7 Magnetic moment

Another interesting physical quantity characterizing the electroweak sphaleron is its magnetic moment μ . The electromagnetic field of the electroweak sphaleron has the asymptotic behaviour

$$\vec{A}_{EM}(\vec{r}) \rightarrow \frac{\vec{\mu} \times \vec{r}}{4\pi r^3}, \quad (32)$$

where $\vec{\mu} = (0, 0, \mu)$ represents the magnetic moment. It can be extracted from the long-range behaviour of the functions $F_3(r, \theta)$, $F_4(r, \theta)$ and $F_7(r, \theta)$. To extract the magnetic moment we perform an (asymptotic) gauge transformation, which changes the asymptotically twisted Higgs field from the ‘Coulomb gauge’ to the ‘physical gauge’, where the Higgs field is asymptotically constant. Applying this transformation to the $SU(2)$ gauge field yields the ‘physical’ asymptotic isospin-3 component of the gauge field, needed to construct the asymptotic behaviour of the electromagnetic field and of the massive Z^0 -field. The magnetic moment consists of a sequence of multipoles

$$\mu = \mu_d + \mu_o \frac{5 \cos^2 \theta - 1}{r^2} + \dots, \quad (33)$$

where the first terms are the dipole moment μ_d and the octupole moment μ_o [18].

2.8 Parameters

Subject to the boundary conditions (25) we solve the equations numerically, using the dimensionless coordinate $x = gvr$. We fix the parameters $g = 0.65$ and $M_W = 80\text{GeV}$. We vary the Higgs mass, though most calculations presented are performed for $M_H = M_W$; and we vary the mixing angle over the full range $0 \leq \theta_w \leq \pi/2$, the physical value being $\theta_w = 0.5$.

3 Multisphaleron solutions

To obtain the multisphaleron solutions we start with the $n = 1$ sphaleron solution as initial guess and increase the value of n successively.

The numerical calculations are based on the Newton-Raphson method. We use the program package FIDISOL [19] which also provides us with an estimate of the discretization errors. The equations are discretized on a grid covering the integration regions $0 \leq x \leq 60$ up to $0 \leq x \leq 180$ and $0 \leq \Theta \leq \pi/2$ with typical grid sizes 50×20 and 100×20 . In most calculations a method with a prescribed grid and order of consistency is used. The estimates of the discretization errors are on the order of 10^{-3} , which suffices to extract the physical quantities with high accuracy. The calculations are more difficult for large Higgs masses, $M_H > 100M_W$. There a method with optimization

of the grid and of the order of consistency is applied [19]. The accuracy of the solution can be thus improved until the estimate of the maximal discretization error is lower than a given limit, e. g. 10^{-3} in our calculations.

3.1 Zero mixing angle

We first present the multisphaleron solutions in the limit of zero mixing angle. In this limit the $U(1)$ field decouples and the function $F_7(x, \theta)$ can consistently be set to zero [11].

Let us now consider the gauge invariant properties of the axially symmetric multisphaleron solutions, the energy, the energy density and the length of the Higgs field. In Fig. 1 we display the energy E of the $n = 5$ multisphaleron, divided by the winding number n , as a function of the Higgs mass and compare it with the energy of the $n = 1$ sphaleron. We also indicate the energy of the $n = 2, 3$ and 4 multisphalerons at several values of the Higgs mass. The energy E of the multisphalerons up to $n = 5$ is also shown in Table 1 for the Higgs masses $M_H = M_W/10$, $M_H = M_W$ and $M_H = 10M_W$ together with the ratio E/n . For small Higgs masses the energy of the multisphalerons is smaller than n times the energy of the sphaleron. For large Higgs masses the energy of the multisphalerons is larger than n times the energy of the sphaleron. Inbetween, at a Higgs mass of $M_H \approx M_W$ the energy of the multisphalerons approximately equals n times the energy of the sphaleron.

In Figs. 2a-2c we show the energy density ϵ , defined by

$$E = \frac{1}{4\pi} \int \epsilon(\vec{x}) x^2 dx \sin \theta d\theta d\phi , \quad (34)$$

where E is the energy in TeV. The energy density is presented along the z -axis, at 45° and along the ρ -axis for the multisphalerons up to $n = 5$ and for the Higgs masses $M_H = M_W/10$, $M_H = M_W$, and $M_H = 10M_W$. The energy density is strongly peaked along the ρ -axis, with the maximum shifting outward with increasing n . Increasing rapidly in size at the origin for increasing Higgs mass, the energy density is localized in a decreasing region of space.

In Figs. 3a-3c we show for the corresponding multisphalerons the magnitude of the Higgs field Φ in units of $v/\sqrt{2}$, denoted by the function $L(x, \theta)$

$$L(x, \theta) = \sqrt{F_5^2(x, \theta) \sin^2 \theta + F_6^2(x, \theta) \cos^2 \theta} . \quad (35)$$

The magnitude of the Higgs field, being zero at the origin, remains small along the ρ -axis for increasingly longer intervals with increasing n . Like the energy density the Higgs field is localized in a decreasing region of space for increasing Higgs mass.

3.2 Finite mixing angle

We now consider the case of finite mixing angle and specify to the Higgs mass $M_H = M_W$.

At finite mixing angle the sphaleron and the multisphalerons possess a magnetic moment. The magnetic moment can be extracted from the asymptotic function $F_7(x, \theta)$ according to [13]

$$\mu = xF_7(x, \theta) \frac{g^2}{e^2} \frac{e}{\alpha_w M_W} . \quad (36)$$

Analyzing the dependence of μ on the angle θ , the dipole moment μ_d and the octupole moment μ_o can be obtained according to Eq. (33). The dipole moment μ_d can be extracted with good accuracy up to the mixing angle $\theta_w = 1.55$, beyond which the function $F_7(x, \theta)$ increases rapidly, leading to large errors on $F_7(x, \theta)$ and making the extraction of μ_d unreliable. The octupole moment μ_o is much smaller than the dipole moment μ_d , and can only be extracted with less accuracy.

3.2.1 Physical mixing angle

We now consider the multisphalerons at the physical mixing angle $\theta_w = 0.5$.

In Table 2 we show the energy (in TeV) of the multisphalerons up to $n = 5$ at the physical mixing angle and compare it to the energy at zero mixing angle (for the Higgs mass $M_H = M_W$). The change in energy due to the finite mixing angle is small, increasing from 1% for $n = 1$ to 2% for $n = 5$.

In Fig. 4 we show the energy density at the physical mixing angle along the z -axis, at 45° and along the ρ -axis for the multisphalerons up to $n = 5$. The change with respect to Fig. 2b, where the energy density at zero mixing angle is shown, is small. At the physical mixing angle the energy density is slightly decreased, most prominently at the maxima along the ρ -axis.

Turning now to the electromagnetic field, we demonstrate in Fig. 5 that the magnetic moment consists dominantly of a dipole moment and an octupole moment. According to Eq. (33) the magnetic moment then has a linear dependence on $\cos^2 \theta$ for a fixed radial coordinate x . From the figure the dipole moment and the octupole moment of the $n = 5$ multisphaleron (for the Higgs mass $M_H = M_W$) can be extracted.

Table 2 gives in addition to the energy the dipole moment μ_d and the octupole moment μ_o for the multisphalerons up to $n = 5$ at the physical mixing angle $\theta_w = 0.5$ (for the Higgs mass $M_H = M_W$). The octupole moment of the sphaleron is very small [18]. It was therefore not extracted in our previous calculations of the sphaleron at finite mixing angle, from where the data for the table are taken [12, 13]. A perturbative calculation of the octupole moment of the sphaleron at the physical mixing angle lead to $\mu_o \approx 10^{-1}e/(\alpha_w M_W^3)$ [18].

The functions $F_i(x, \theta)$ are gauge dependent quantities. Nevertheless we show as an example the functions $F_i(x, \theta)$ for the $n = 5$ multisphaleron at the physical mixing angle $\theta_w = 0.5$ (for the Higgs mass $M_H = M_W$) in Figs. 6a-6d.

3.2.2 Mixing angle dependence

We now demonstrate the dependence of the multisphalerons on the mixing angle over the full range of the mixing angle $0 \leq \theta_w \leq \pi/2$.

In Fig. 7 we show the energy of the $n = 5$ multisphaleron as a function of the mixing angle and the energy of the $n = 2, 3$ and 4 multisphalerons at the mixing angles $\theta_w = 0, 0.5$ and 1.0 . The figure also gives the energy of the sphaleron for comparison [13]. With increasing mixing angle θ_w the energy decreases monotonically. Approaching the limiting value $\theta_w = \pi/2$ the energy of the $n = 5$ multisphaleron smoothly approaches a limiting value. This is in contrast to the sphaleron, whose energy decreases strongly, when $\theta_w \rightarrow \pi/2$. (Though recall, that the numerics becomes less reliable in the limit $\theta_w \rightarrow \pi/2$.)

The energy density is presented in Figs. 8a-8b. In Fig. 8a we show the energy density for the multisphalerons up to $n = 5$ at the mixing angle $\theta_w = 1$. Comparing this figure with Fig. 4 we observe a further decrease of the energy density. In Fig. 8b we show the energy density of the $n = 5$ multisphaleron for the mixing angles $\theta_w = 0.5, 1.0, 1.5$ and 1.55 . While the energy density decreases monotonically with increasing mixing angle, the maximum along the ρ -axis remains almost fixed.

In Fig. 9 we present the dipole moment as a function of the mixing angle for the $n = 5$ multisphaleron. We also show the dipole moment of the $n = 2, 3$ and 4 multisphalerons at the mixing angles $\theta_w = 0.5$ and 1.0 . For comparison the dipole moment of the sphaleron is also shown [13]. We observe, that the dipole moment of the multisphalerons is on the order of n times the dipole moment of the sphaleron, for all mixing angles.

Table 3 summarizes the energy, the dipole moment and the octupole moment of the $n = 2, 3, 4$ and 5 multisphalerons at the mixing angle $\theta_w = 1.0$.

4 Conclusions

We have constructed multisphaleron solutions in the electroweak interactions. The multisphaleron solutions have axial symmetry and parity reflection symmetry. At zero mixing angle, where the sphaleron is spherically symmetric, the multisphalerons are only axially symmetric, too.

The multisphaleron solutions are characterized by an integer n , related to the winding of the fields in the azimuthal angle ϕ . With increasing n the energy density of the

multisphalerons becomes increasingly deformed, the maximum of the energy density occurring along the ρ -axis at increasing distance from the origin.

The energy of the multisphalerons is on the order of n times the sphaleron energy. For small Higgs masses the energy of the multisphalerons is less than n times the energy of the sphaleron, $E(n) < nE(1)$, while for large Higgs masses the energy of the multisphalerons is greater than n times the energy of the sphaleron, $E(n) > nE(1)$. Inbetween, at a Higgs mass of $M_H \approx M_W$ the energy of the multisphalerons approximately equals n times the energy of the sphaleron.

At the physical mixing angle the multisphaleron solutions differ only little from the solutions at zero mixing angle, except that the $U(1)$ field is finite. Compared to zero mixing angle the energy is only smaller by 1% for the sphaleron and by 2% for the $n = 5$ multisphaleron at the physical mixing angle. Like the sphaleron the multisphalerons have large magnetic dipole moments, being on the order of n times the dipole moment of the sphaleron. Their octupole moments are small and negative.

The sphaleron represents the maximal energy configuration along a non-contractible loop with winding number $n = 1$, its Chern-Simons charge is given by $N_{CS} = 1/2$. The multisphaleron solutions have Chern-Simons charge $N_{CS} = n/2$. We conclude, that symmetric non-contractible loops can be constructed, leading from the vacuum with Chern-Simons charge $N_{CS} = 0$ to topologically distinct vacua with Chern-Simons charge $N_{CS} = n$, passing the multisphaleron solutions with $N_{CS} = n/2$ midway.

At finite temperature such paths involving multisphalerons should allow for thermal fermion number violating transitions, which would correspond to tunnelling transitions via multiinstantons at zero temperature. Since multiinstantons with winding number n possess n fermion zero modes, we expect to encounter n fermion zero modes along vacuum to vacuum paths, passing the n -th multisphaleron. Though relevant in principle for baryon number violating processes, the multisphalerons have much higher energies than the sphaleron, making such processes much more unlikely and therefore less relevant for cosmology and for the baryon asymmetry of the universe.

Acknowledgement

We gratefully acknowledge discussions with Yves Brihaye.

References

- [1] G. 't Hooft, Symmetry breaking through Bell-Jackiw Anomalies, *Phys. Rev. Lett.* 37 (1976) 8.
- [2] A. Ringwald, High energy breakdown of perturbation theory in the electroweak instanton sector, *Nucl. Phys.* B330 (1990) 1.
- [3] M. Mattis, and E. Mottola, eds., “Baryon Number Violation at the SSC?”, World Scientific, Singapore (1990).
- [4] N. S. Manton, Topology in the Weinberg-Salam theory, *Phys. Rev.* D28 (1983) 2019.
- [5] F. R. Klinkhamer, and N. S. Manton, A saddle-point solution in the Weinberg-Salam theory, *Phys. Rev.* D30 (1984) 2212.
- [6] V. A. Kuzmin, V. A. Rubakov, and M. E. Shaposhnikov, On anomalous electroweak baryon-number non-conservation in the early universe, *Phys. Lett.* B155 (1985) 36.
- [7] P. Arnold, and L. McLerran, Sphalerons, small fluctuations, and baryon-number violation in electroweak theory, *Phys. Rev.* D36 (1987) 581.
- [8] P. Arnold, and L. McLerran, The sphaleron strikes back: A response to objections to the sphaleron approximation, *Phys. Rev.* D37 (1988) 1020.
- [9] L. Carson, X. Li, L. McLerran, and R.-T. Wang, Exact computation of the small-fluctuation determinant around a sphaleron, *Phys. Rev.* D42 (1990) 2127.
- [10] E. W. Kolb, and M. S. Turner, “The Early Universe”, Addison-Wesley Publishing Company, Redwood City (1990).
- [11] B. Kleihaus, and J. Kunz, Multisphalerons in the weak interactions, *Phys. Lett.* B (1994) in press.
- [12] B. Kleihaus, J. Kunz, and Y. Brihaye, The electroweak sphaleron at physical mixing angle, *Phys. Lett.* B273 (1991) 100.
- [13] J. Kunz, B. Kleihaus, and Y. Brihaye, Sphalerons at finite mixing angle, *Phys. Rev.* D46 (1992) 3587.
- [14] N. S. Manton, Complex structure of monopoles, *Nucl. Phys.* B135 (1978) 319.
- [15] C. Rebbi, and P. Rossi, Multimonopole solutions in the Prasad-Sommerfield limit, *Phys. Rev.* D22 (1980) 2010.

- [16] Y. Brihaye, B. Kleihaus, and J. Kunz, Sphalerons at finite mixing angle and singular gauges, *Phys. Rev. D*47 (1993) 1664.
- [17] Y. Brihaye, and J. Kunz, On axially symmetric solutions in the electroweak theory, preprint THU-94/7.
- [18] M. E. R. James, The sphaleron at non-zero Weinberg angle, *Z. Phys. C*55 (1992) 515.
- [19] W. Schönauer, and R. Weiß, Efficient vectorizable PDE solvers, *J. Comp. and Appl. Math.* 27 (1989) 279;
W. Schönauer, E. Schnepf, and H. Müller, The FIDISOL Program Package, *Intern. Bericht 27/85* des Rechenzentrums der Universität Karlsruhe.

5 Tables

Table 1

$E(n)$ [TeV] ($E(n)/n$ [TeV])

n	$M_H = M_W/10$	$M_H = M_W$	$M_H = 10M_W$
1	7.468 (7.468)	8.665 (8.665)	11.375 (11.375)
2	13.791 (6.896)	17.140 (8.570)	24.937 (12.469)
3	19.881 (6.627)	25.879 (8.626)	40.030 (13.343)
4	25.908 (6.477)	34.931 (8.733)	56.298 (14.075)
5	31.931 (6.386)	44.288 (8.858)	73.521 (14.704)

Table 1:

The energy E (in TeV) and the energy E (in TeV) divided by the winding number n are shown for the sphaleron and the multisphalerons up to $n = 5$ for the Higgs masses $M_H = M_W/10$, $M_H = M_W$ and $M_H = 10M_W$ for zero mixing angle.

Table 2

$\theta_w = 0.5$, $M_H = M_W$

n	E [TeV]	$E(0.5)/E(0)$	μ_d [$e/(\alpha_w M_W)$]	μ_o [$e/(\alpha_w M_W^3)$]
1	8.587	0.991	1.779	
2	16.923	0.987	3.725	-2.
3	25.475	0.984	5.947	-7.
4	34.294	0.982	8.420	-14.
5	43.374	0.979	11.116	-24.

Table 2:

The energy E (in TeV), the ratio of the energy at the physical mixing angle $\theta_w = 0.5$ to the energy at zero mixing angle $\theta_w = 0$, the magnetic dipole moment μ_d (in units of $[e/(\alpha_w M_W)]$) and the magnetic octupole moment μ_o (in units of $[e/(\alpha_w M_W^3)]$) are shown for the sphaleron and the multisphalerons up to $n = 5$ for the Higgs mass $M_H = M_W$ and for the physical mixing angle $\theta_w = 0.5$. (The magnetic octupole moment μ_o was not extracted in [13].)

Table 3

$$\theta_w = 1.0, M_H = M_W$$

n	E [TeV]	$E(1.0)/E(0)$	μ_d [$e/(\alpha_w M_W)$]	μ_o [$e/(\alpha_w M_W^3)$]
1	8.295	0.957	1.848	
2	16.179	0.944	3.835	-3.
3	24.169	0.934	6.051	-7.
4	32.327	0.925	8.490	-15.
5	40.659	0.918	11.116	-25.

Table 3:

Idem Table 2 for the mixing angle $\theta_w = 1.0$.

6 Figure captions

Figure 1:

The energy E (in TeV), divided by the winding number n , is shown as a function of the Higgs mass M_H (in units of M_W) for zero mixing angle for the sphaleron and the $n = 5$ multisphaleron (solid lines), the $n = 2$ multisphaleron (crosses), the $n = 3$ multisphaleron (asterisks), and the $n = 4$ multisphaleron (plus signs).

Figure 2a:

The energy density $\epsilon(x, \theta)$ (in TeV) is shown as a function of the dimensionless coordinate x for the Higgs mass $M_H = M_W/10$ and for zero mixing angle for the sphaleron and the multisphalerons up to $n = 5$ along the z -axis at $\theta = 0^\circ$ (dashed), at $\theta = 45^\circ$ (dotted), and along the ρ -axis at $\theta = 90^\circ$ (solid).

Figure 2b:

Idem Fig. 2a for the Higgs mass $M_H = M_W$.

Figure 2c:

Idem Fig. 2a for the Higgs mass $M_H = 10M_W$. The density profile along the z -axis and at $\theta = 45^\circ$ becomes steeper with increasing winding number n .

Figure 3a:

The magnitude of the Higgs field $L(x, \theta)$ (in units of $v/\sqrt{2}$) is shown as a function of the dimensionless coordinate x for the Higgs mass $M_H = M_W/10$ and for zero mixing angle for the sphaleron and the multisphalerons up to $n = 5$ along the z -axis at $\theta = 0^\circ$ (dashed), and along the ρ -axis at $\theta = 90^\circ$ (solid). Both, along the z -axis and along the ρ -axis, the curves become flatter with increasing winding number n .

Figure 3b:

Idem Fig. 3a for the Higgs mass $M_H = M_W$.

Figure 3c:

Idem Fig. 3a for the Higgs mass $M_H = 10M_W$. But with increasing winding number n , the curves become steeper along the z -axis, while they become flatter along the ρ -axis.

Figure 4:

The energy density $\epsilon(x, \theta)$ (in TeV) is shown as a function of the dimensionless coordinate x for the Higgs mass $M_H = M_W$ and for the physical mixing angle $\theta_w = 0.5$ for the sphaleron and the multisphalerons up to $n = 5$ along the z -axis at $\theta = 0^\circ$ (dashed), at $\theta = 45^\circ$ (dotted), and along the ρ -axis at $\theta = 90^\circ$ (solid).

Figure 5:

The magnetic moment μ (in units of $e/(\alpha_w M_W)$), is shown as a function of $\cos^2 \theta$ for the Higgs mass $M_H = M_W$ and for the physical mixing angle $\theta_w = 0.5$ for the $n = 5$ multisphaleron for the values of the dimensionless coordinate $x = 60$ (dash-dotted), $x = 72$ (dashed), $x = 84$ (dotted), and $x = 96$ (solid).

Figure 6a:

The $SU(2)$ gauge field functions $F_1(x, \theta)$ and $F_2(x, \theta)$ are shown as a function of the dimensionless coordinate x for the Higgs mass $M_H = M_W$ and for the physical mixing angle $\theta_w = 0.5$ for the $n = 5$ multisphaleron along the z -axis at $\theta = 0^\circ$ (dashed), at $\theta = 45^\circ$ (dotted), and along the ρ -axis at $\theta = 90^\circ$ (solid).

Figure 6b:

Idem Fig. 6a for the $SU(2)$ gauge field functions $F_3(x, \theta)$ and $F_4(x, \theta)$.

Figure 6c:

Idem Fig. 6a for the Higgs field functions $F_5(x, \theta)$ and $F_6(x, \theta)$.

Figure 6d:

Idem Fig. 6a for the magnitude of the Higgs field $L(x, \theta)$ and the $U(1)$ gauge field function $F_7(x, \theta)$.

Figure 7:

The energy E (in TeV), divided by the winding number n , is shown as a function of the mixing angle θ_w for the Higgs mass $M_H = M_W$ for the sphaleron and the $n = 5$ multisphaleron (solid lines), the $n = 2$ multisphaleron (crosses), the $n = 3$ multisphaleron (asterisks), and the $n = 4$ multisphaleron (plus signs).

Figure 8a:

The energy density $\epsilon(x, \theta)$ (in TeV) is shown as a function of the dimensionless coordinate x for the Higgs mass $M_H = M_W$ and for the mixing angle $\theta_w = 1.0$ for the sphaleron and the multisphalerons up to $n = 5$ along the z -axis at $\theta = 0^\circ$ (dashed), at $\theta = 45^\circ$ (dotted), and along the ρ -axis at $\theta = 90^\circ$ (solid).

Figure 8b:

The energy density $\epsilon(x, \theta)$ (in TeV) is shown as a function of the dimensionless coordinate x for the Higgs mass $M_H = M_W$ for the $n = 5$ multisphaleron for the mixing angles $\theta_w = 0.5$ (solid), $\theta_w = 1.0$ (dot-dashed), $\theta_w = 1.5$ (dotted), and $\theta_w = 1.55$ (dashed), along the z -axis at $\theta = 0^\circ$, at $\theta = 45^\circ$, and along the ρ -axis at $\theta = 90^\circ$, $\epsilon(x, \theta)$ is monotonically increasing with increasing angle.

Figure 9:

The magnetic dipole moment μ_d (in units of $e/(\alpha_w M_W)$), divided by the winding number n , is shown as a function of the mixing angle θ_w for the Higgs mass $M_H = M_W$ for the sphaleron and the $n = 5$ multisphaleron (solid lines), the $n = 2$ multisphaleron (crosses), the $n = 3$ multisphaleron (asterisks), and the $n = 4$ multisphaleron (plus signs).

This figure "fig1-1.png" is available in "png" format from:

<http://arXiv.org/ps/hep-ph/9405387v1>

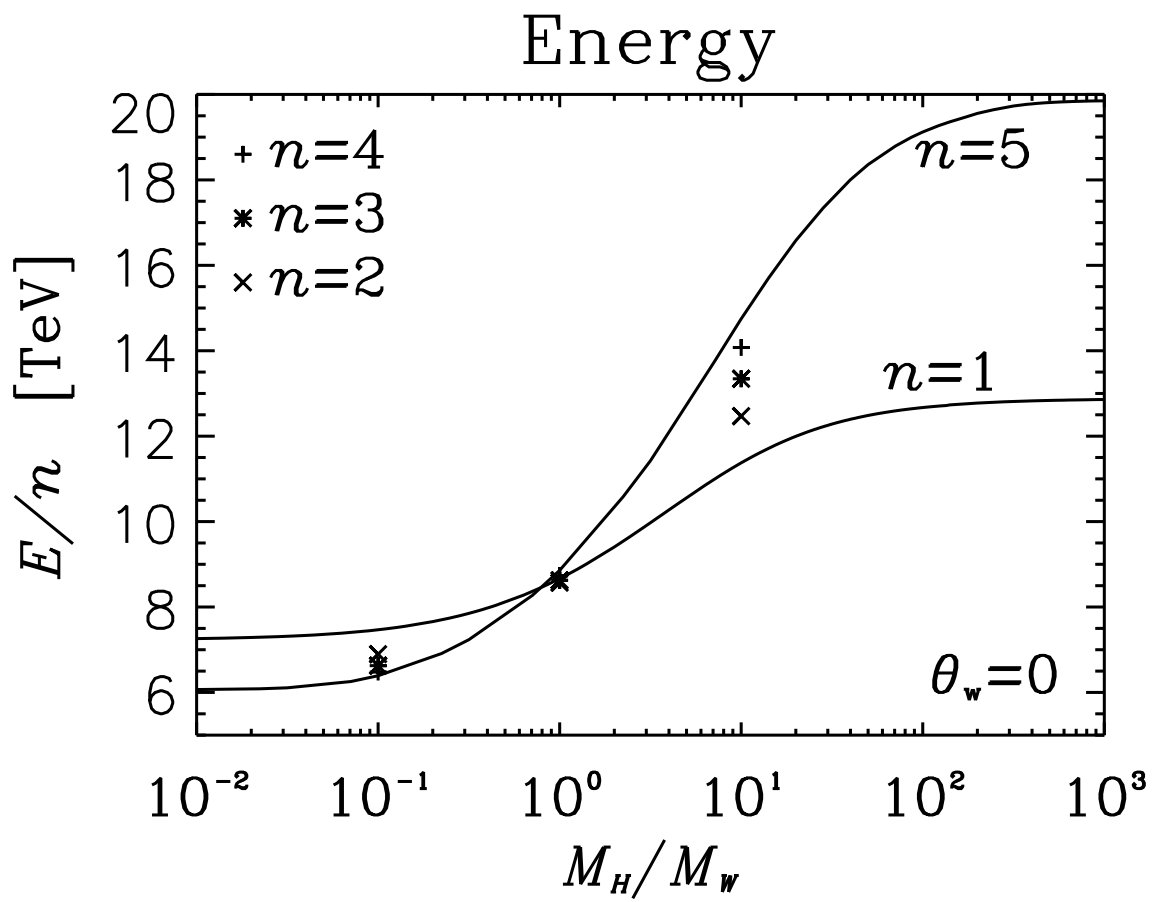


Figure 1

This figure "fig2-1.png" is available in "png" format from:

<http://arXiv.org/ps/hep-ph/9405387v1>

This figure "fig3-1.png" is available in "png" format from:

<http://arXiv.org/ps/hep-ph/9405387v1>

This figure "fig1-2.png" is available in "png" format from:

<http://arXiv.org/ps/hep-ph/9405387v1>

This figure "fig2-2.png" is available in "png" format from:

<http://arXiv.org/ps/hep-ph/9405387v1>

Energy density

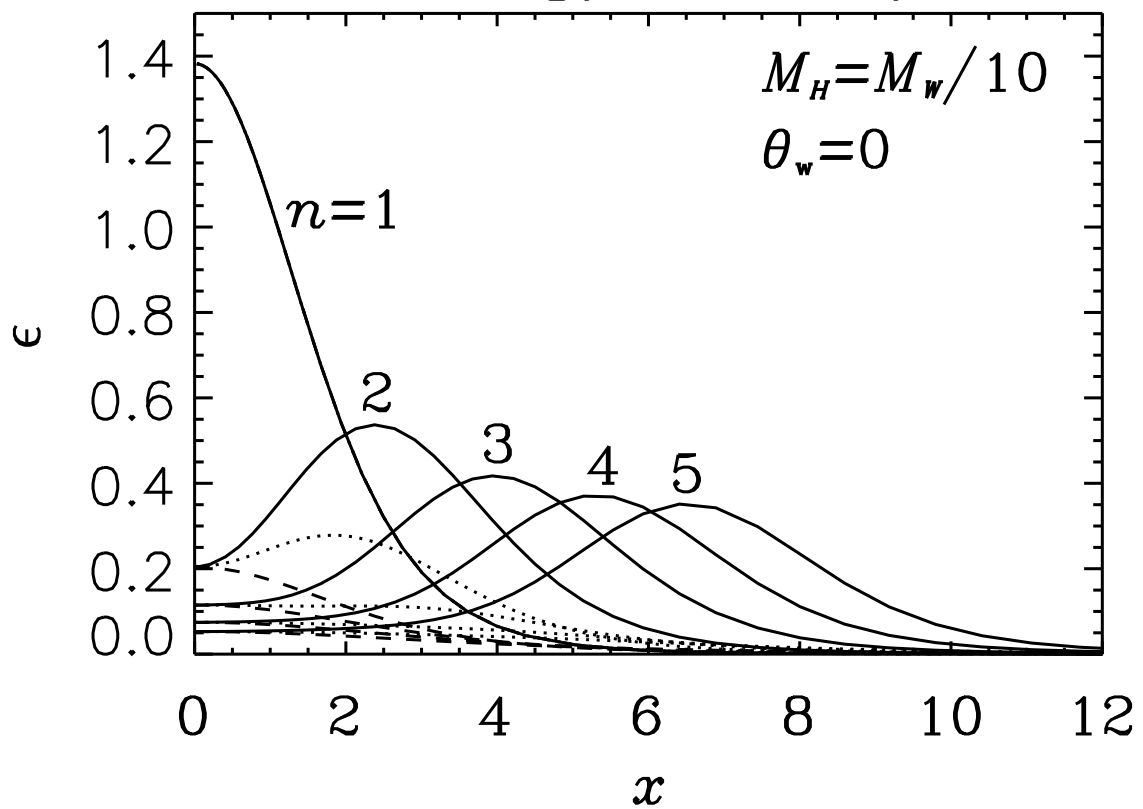


Figure 2a

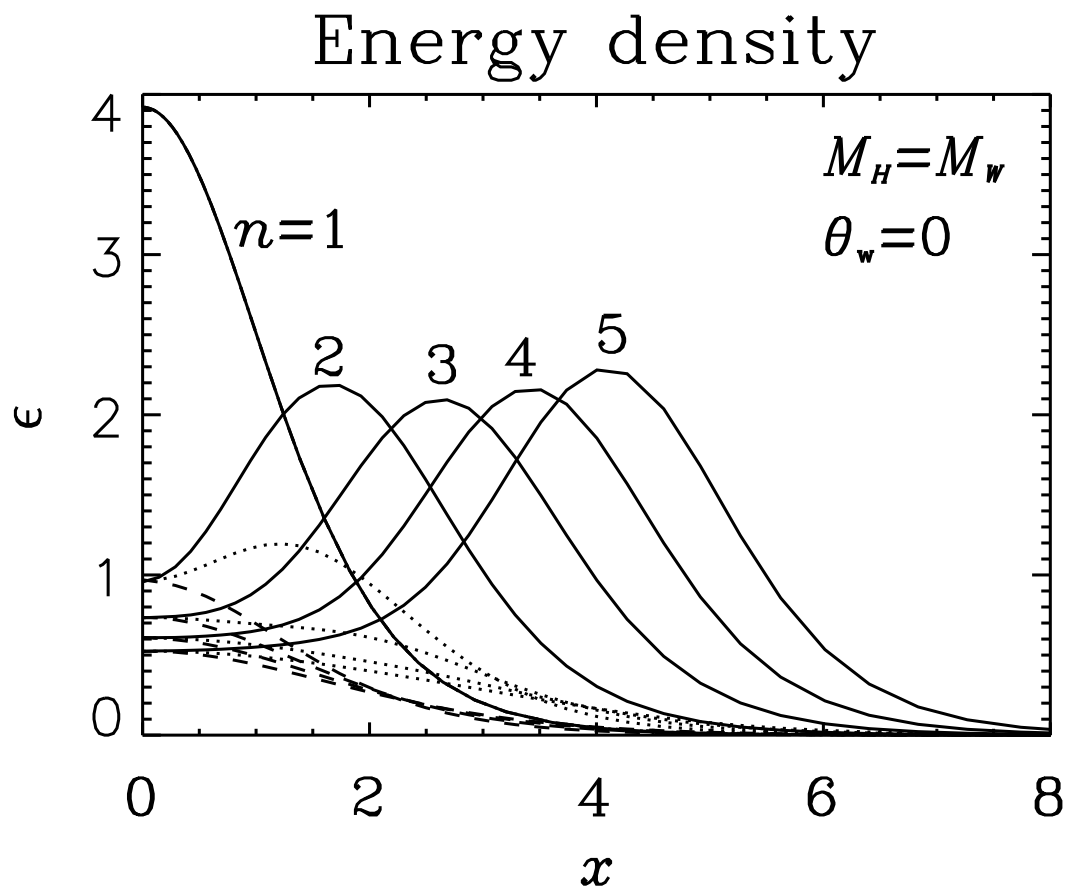


Figure 2b

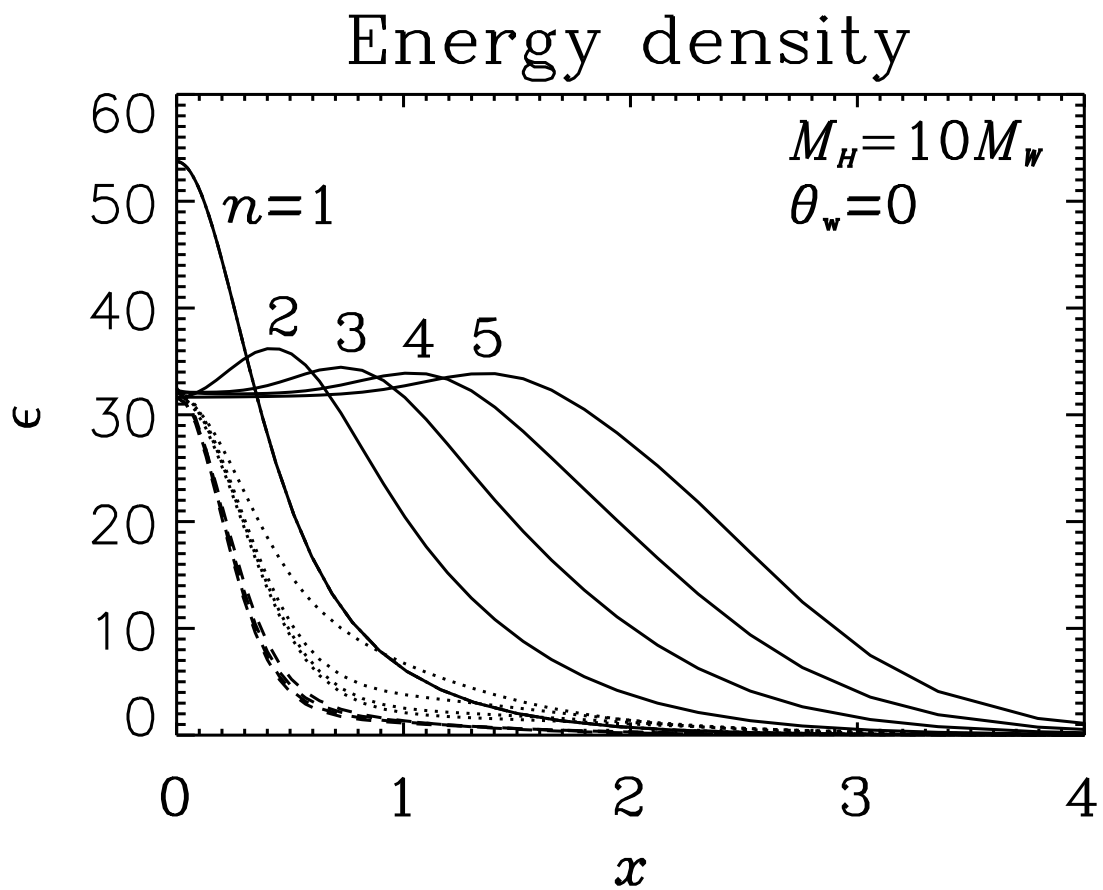


Figure 2c

This figure "fig3-2.png" is available in "png" format from:

<http://arXiv.org/ps/hep-ph/9405387v1>

This figure "fig1-3.png" is available in "png" format from:

<http://arXiv.org/ps/hep-ph/9405387v1>

This figure "fig2-3.png" is available in "png" format from:

<http://arXiv.org/ps/hep-ph/9405387v1>

This figure "fig3-3.png" is available in "png" format from:

<http://arXiv.org/ps/hep-ph/9405387v1>

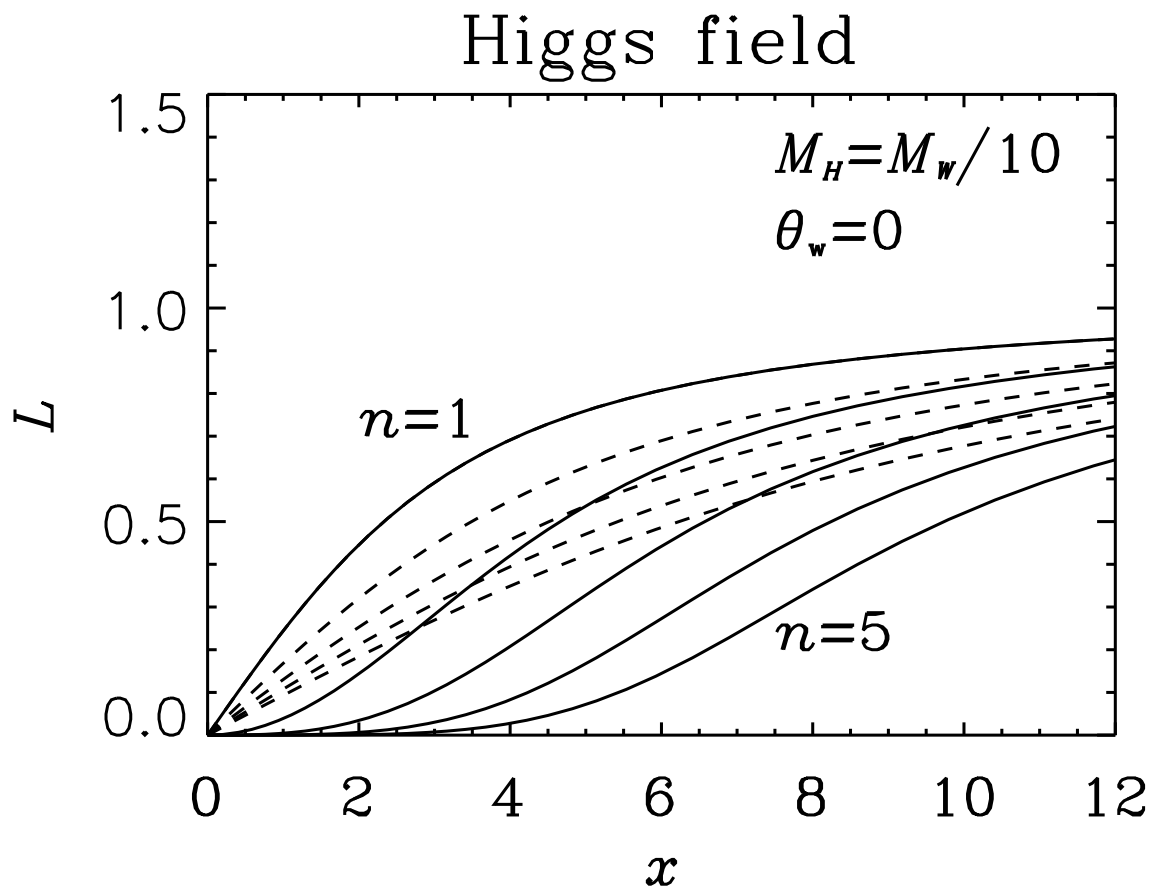


Figure 3a

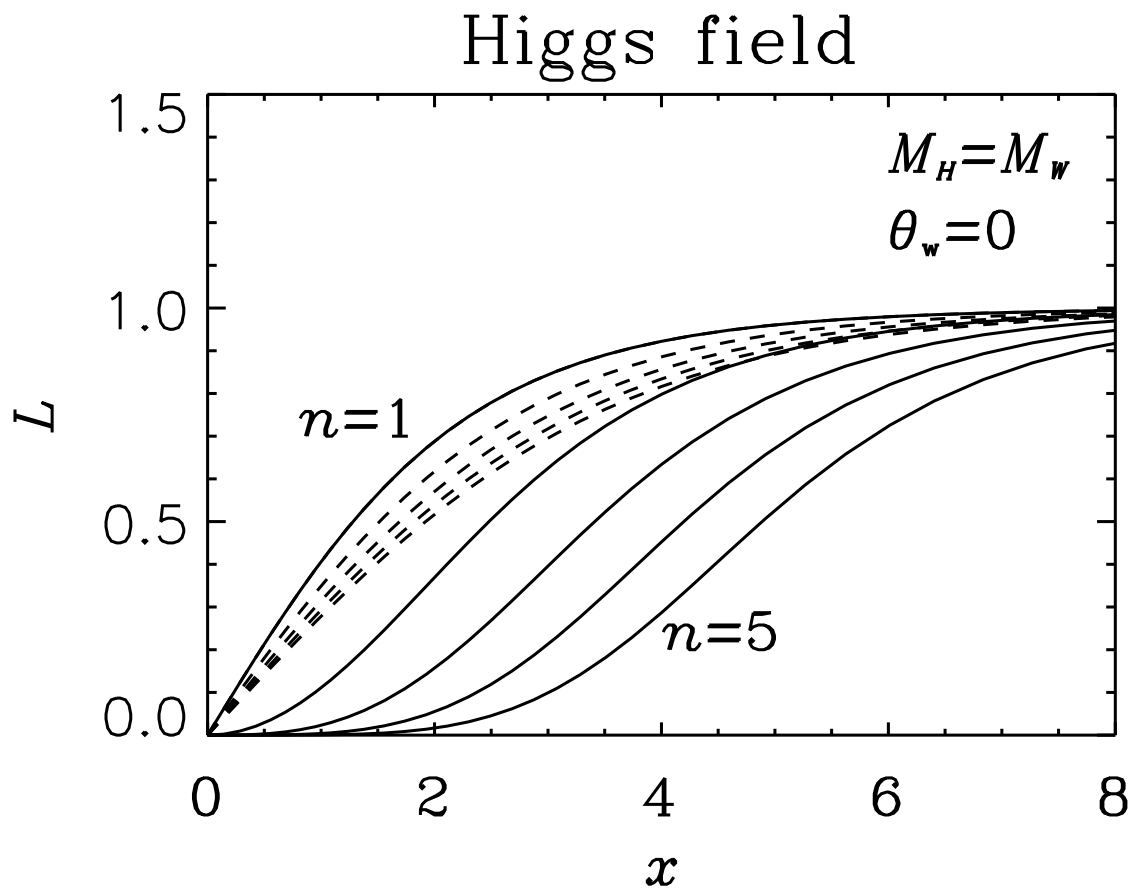


Figure 3b

Higgs field

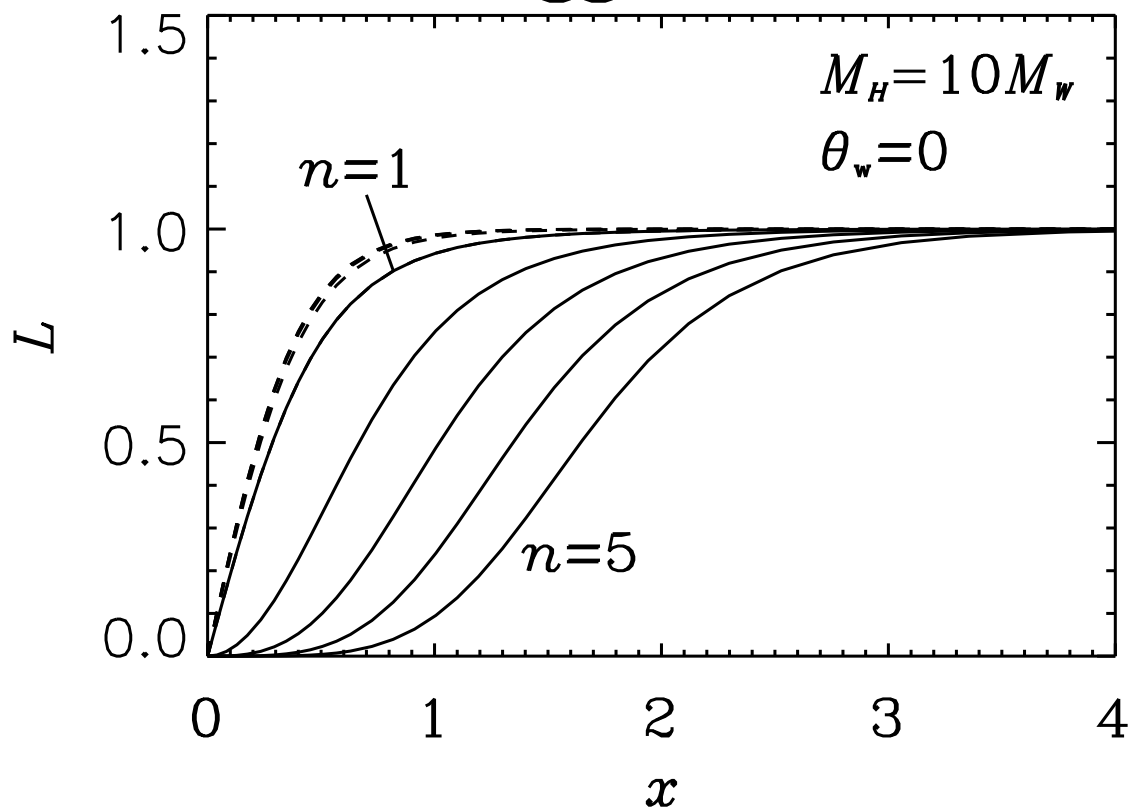


Figure 3c

This figure "fig1-4.png" is available in "png" format from:

<http://arXiv.org/ps/hep-ph/9405387v1>

This figure "fig2-4.png" is available in "png" format from:

<http://arXiv.org/ps/hep-ph/9405387v1>

This figure "fig3-4.png" is available in "png" format from:

<http://arXiv.org/ps/hep-ph/9405387v1>

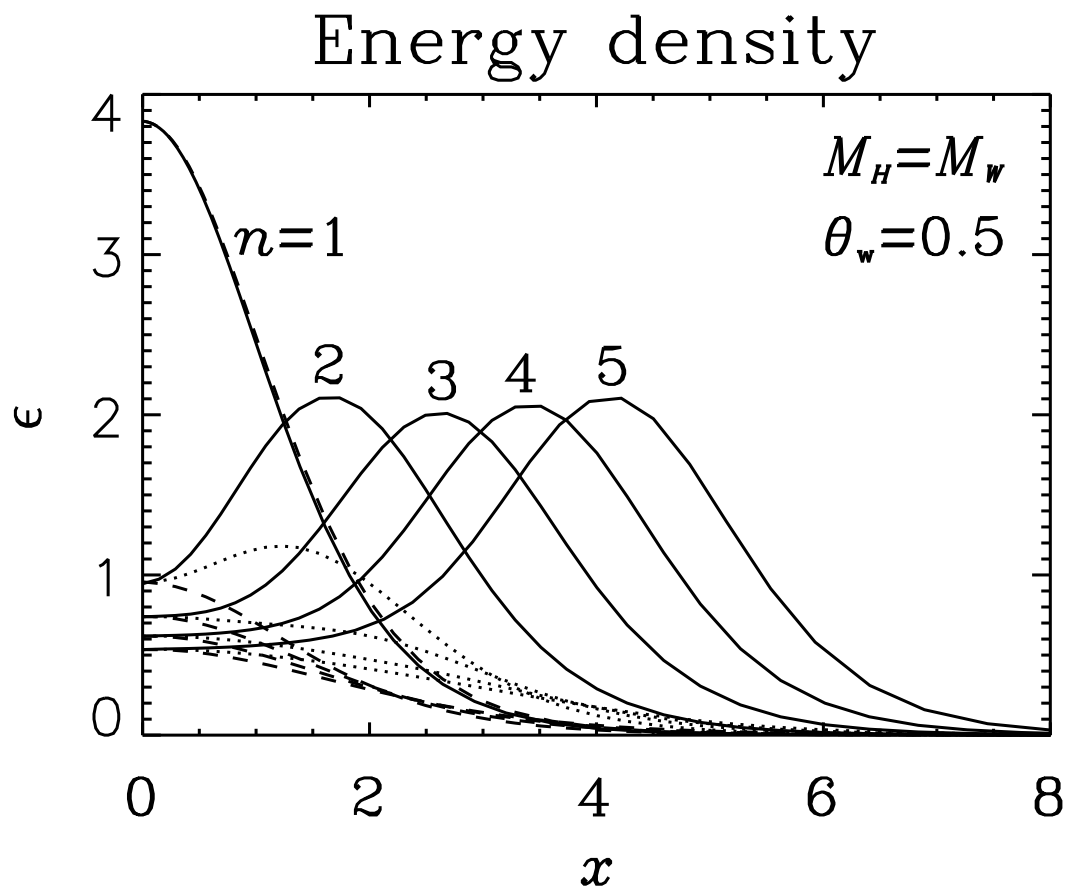


Figure 4

This figure "fig1-5.png" is available in "png" format from:

<http://arXiv.org/ps/hep-ph/9405387v1>

This figure "fig2-5.png" is available in "png" format from:

<http://arXiv.org/ps/hep-ph/9405387v1>

This figure "fig3-5.png" is available in "png" format from:

<http://arXiv.org/ps/hep-ph/9405387v1>

Magnetic moment

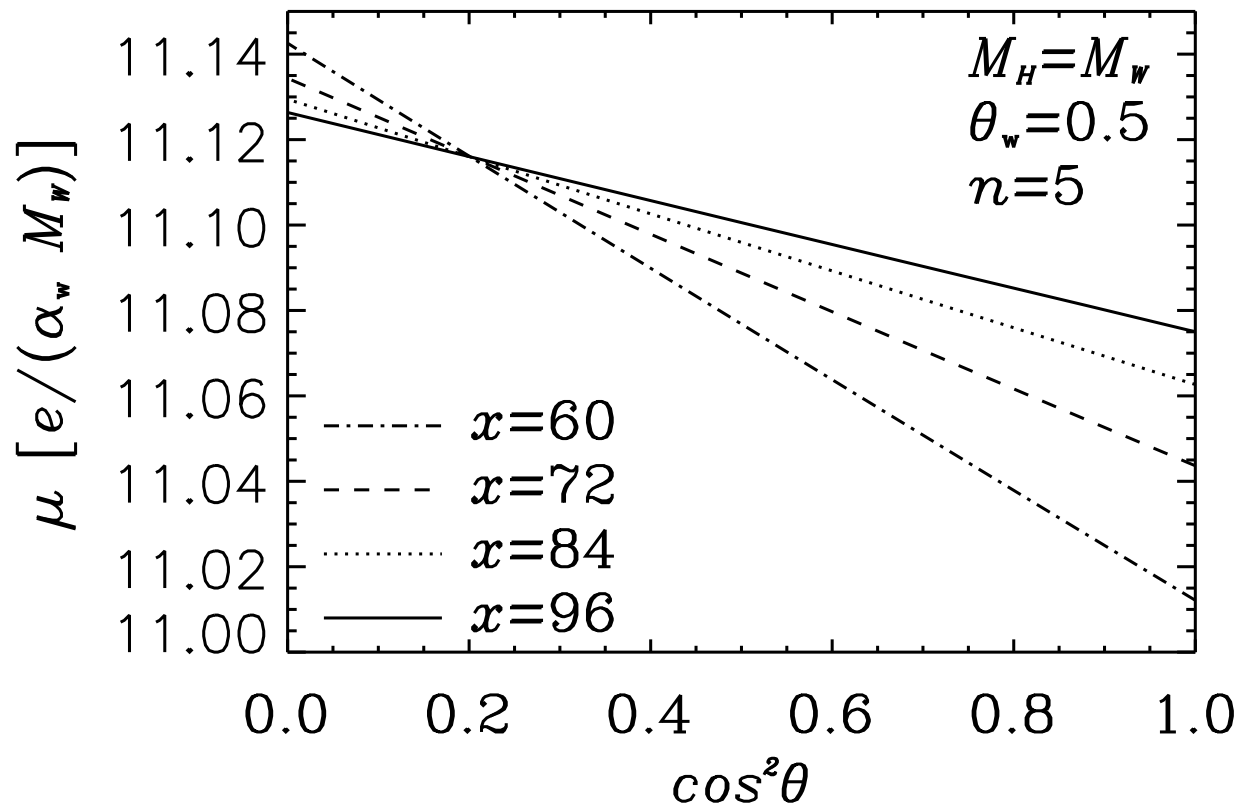


Figure 5

This figure "fig1-6.png" is available in "png" format from:

<http://arXiv.org/ps/hep-ph/9405387v1>

This figure "fig2-6.png" is available in "png" format from:

<http://arXiv.org/ps/hep-ph/9405387v1>

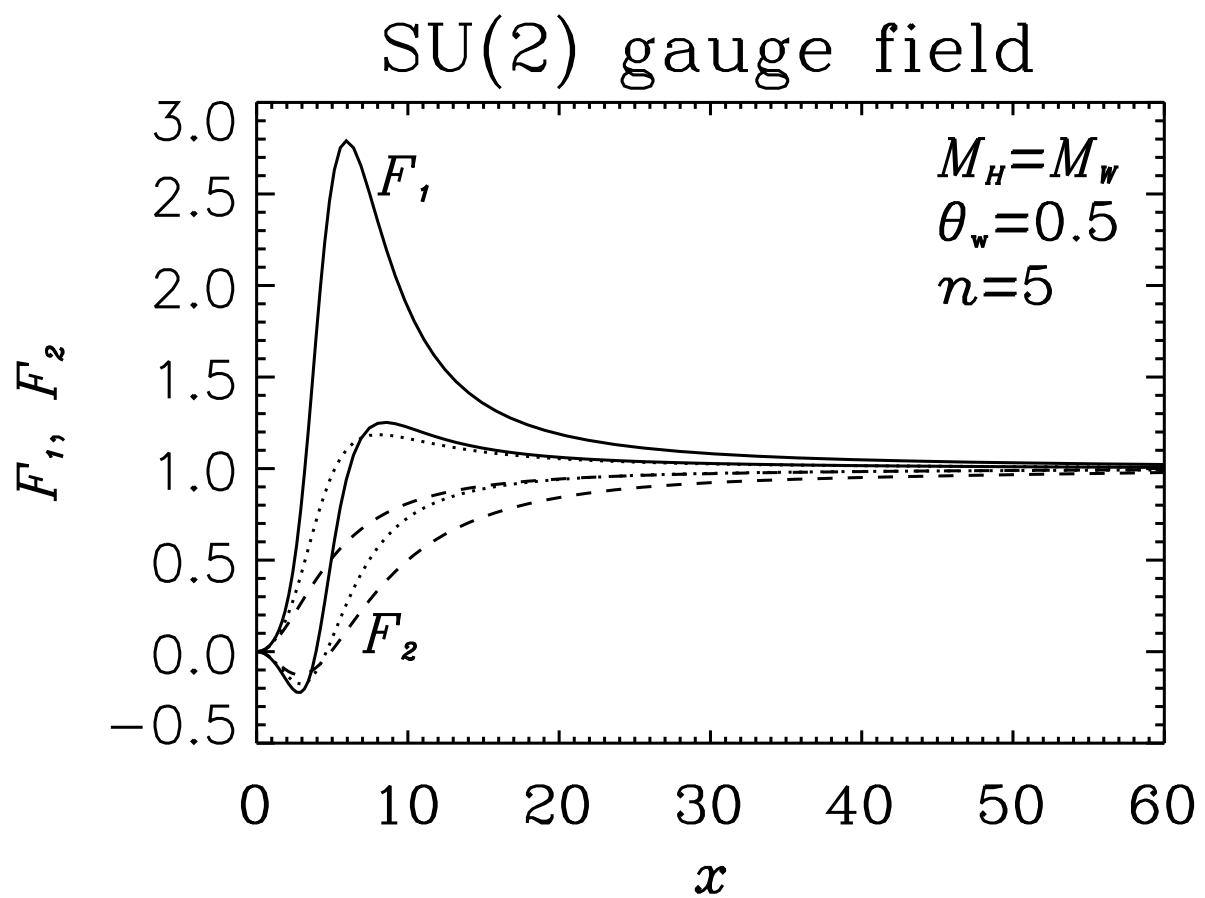


Figure 6a

SU(2) gauge field

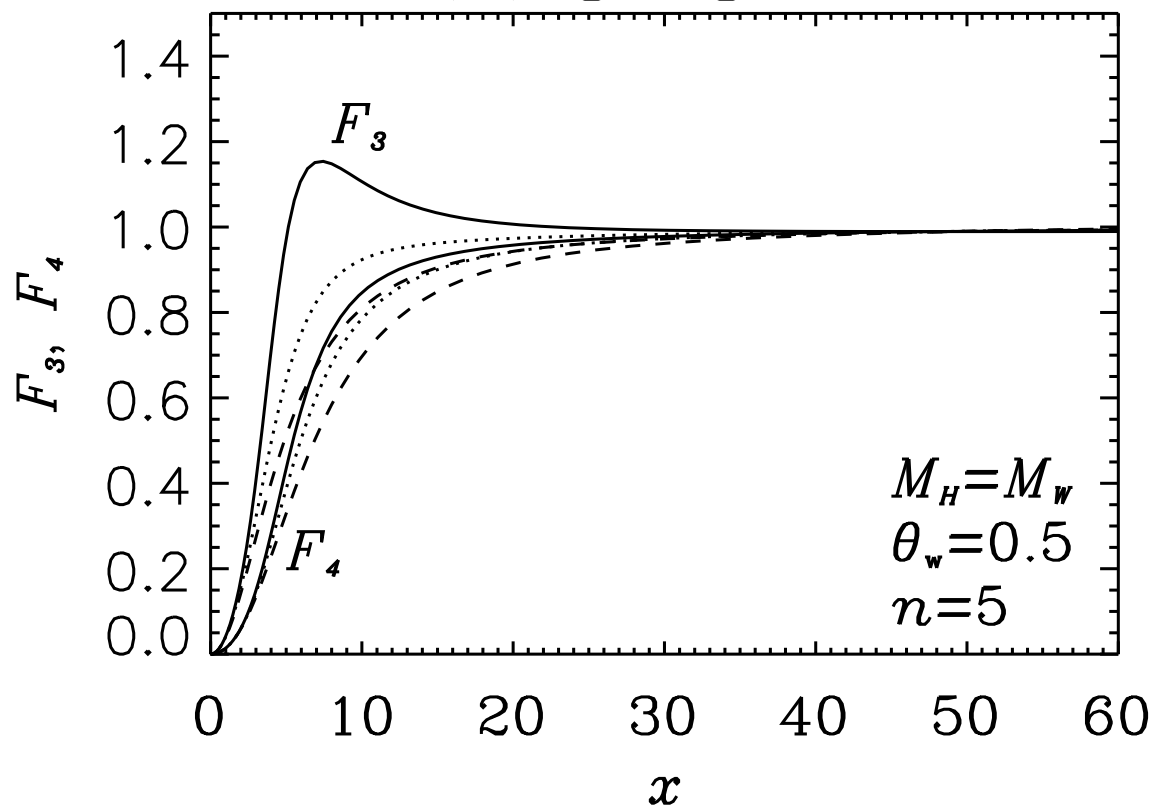


Figure 6b

Higgs field

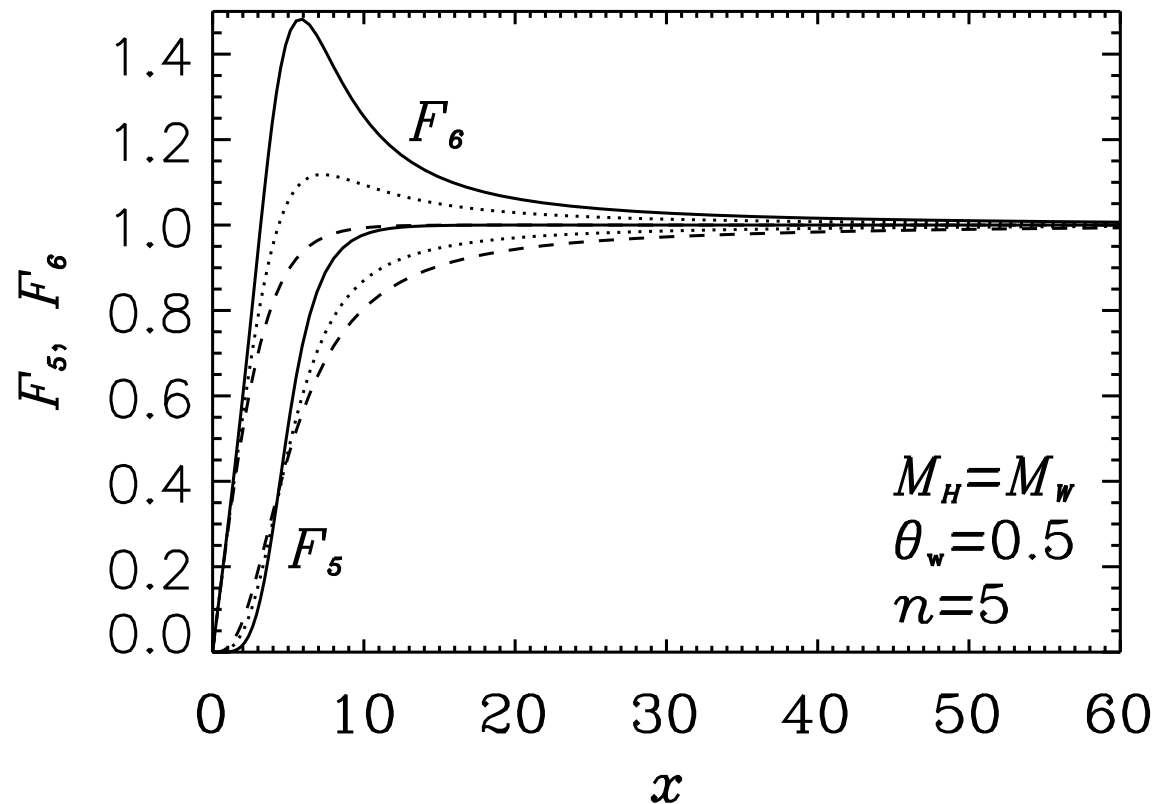


Figure 6c

Higgs field and $U(1)$ field

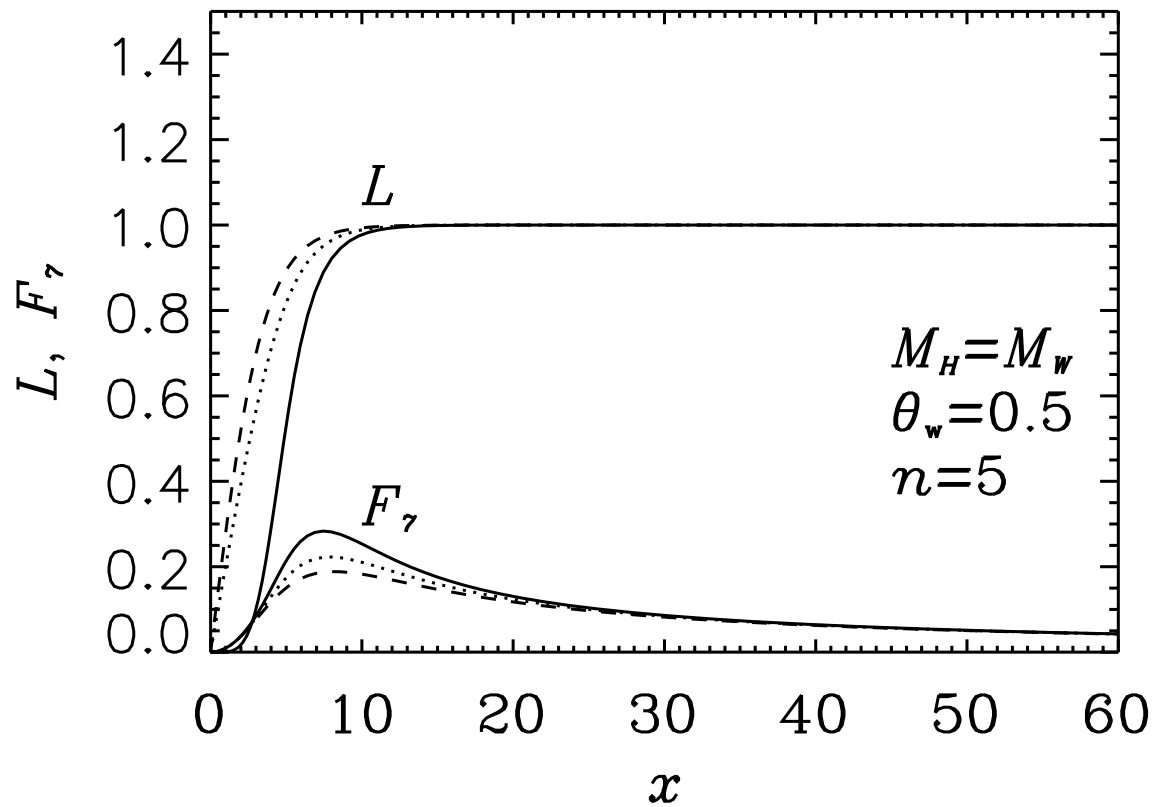


Figure 6d

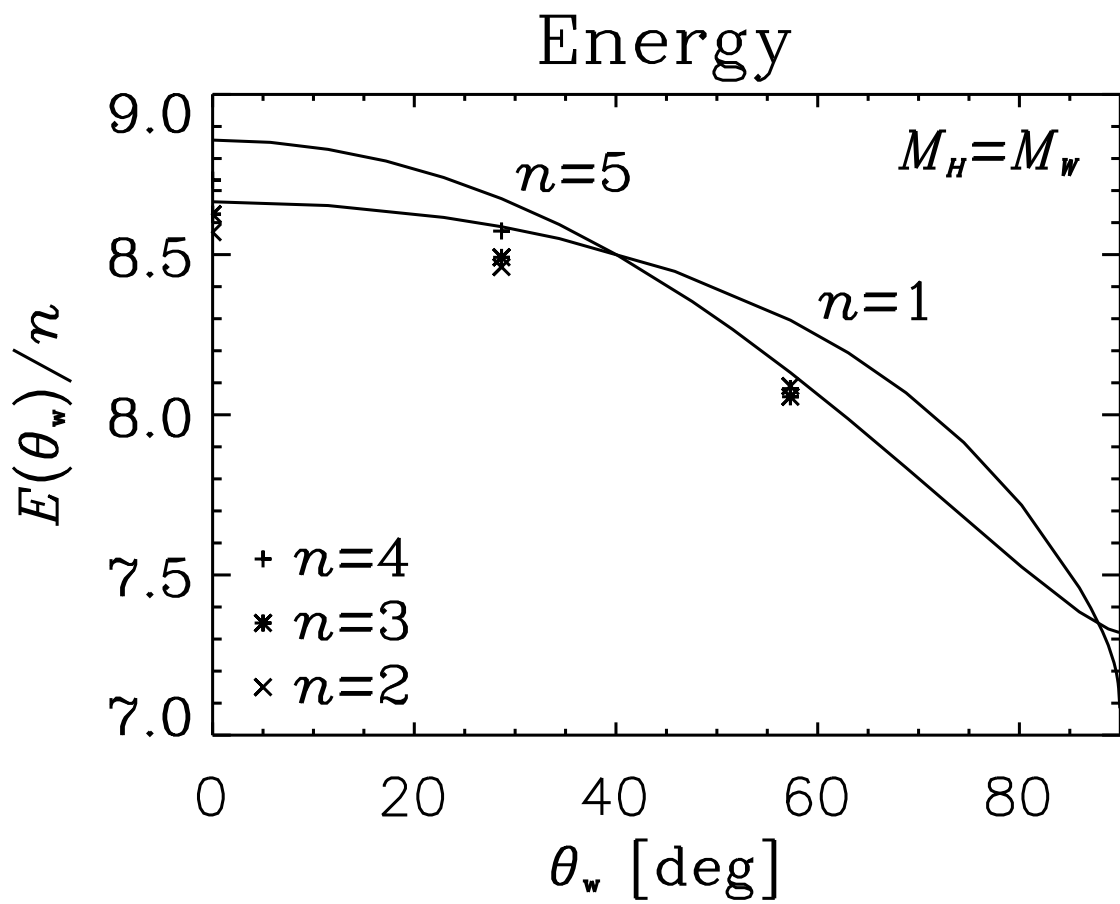


Figure 7

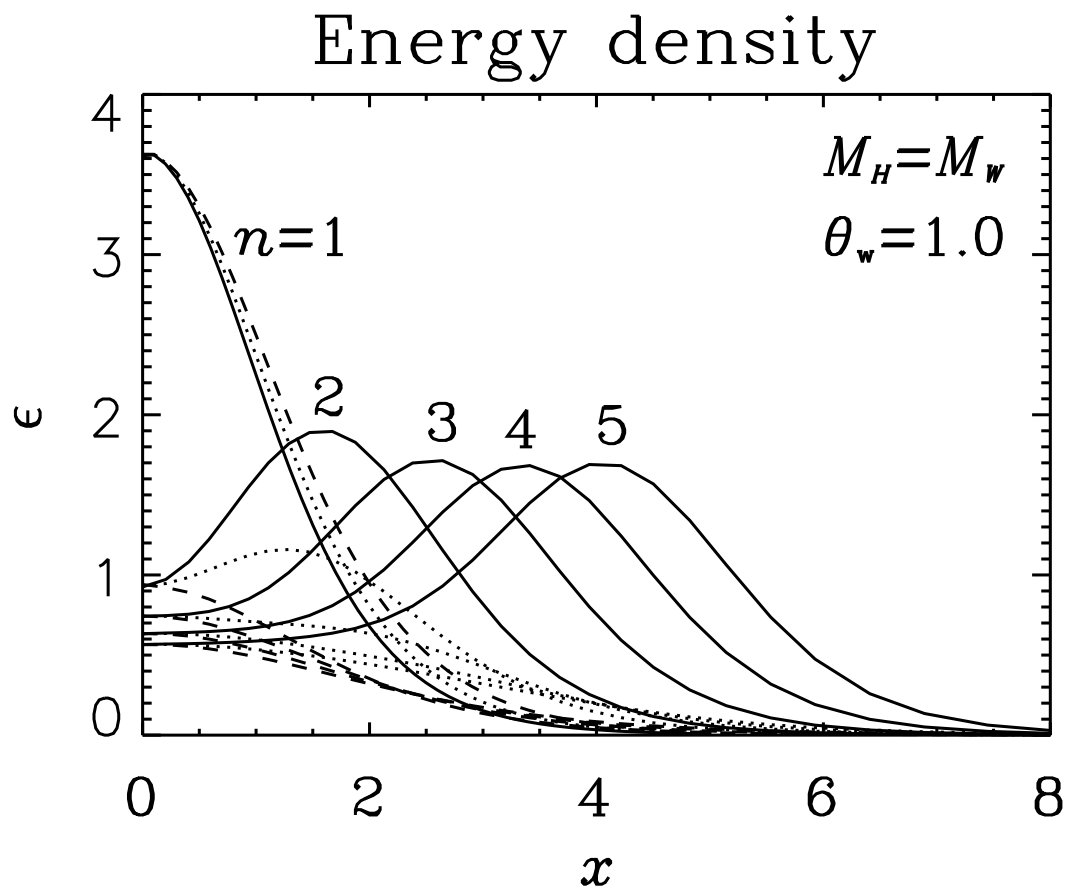


Figure 8a

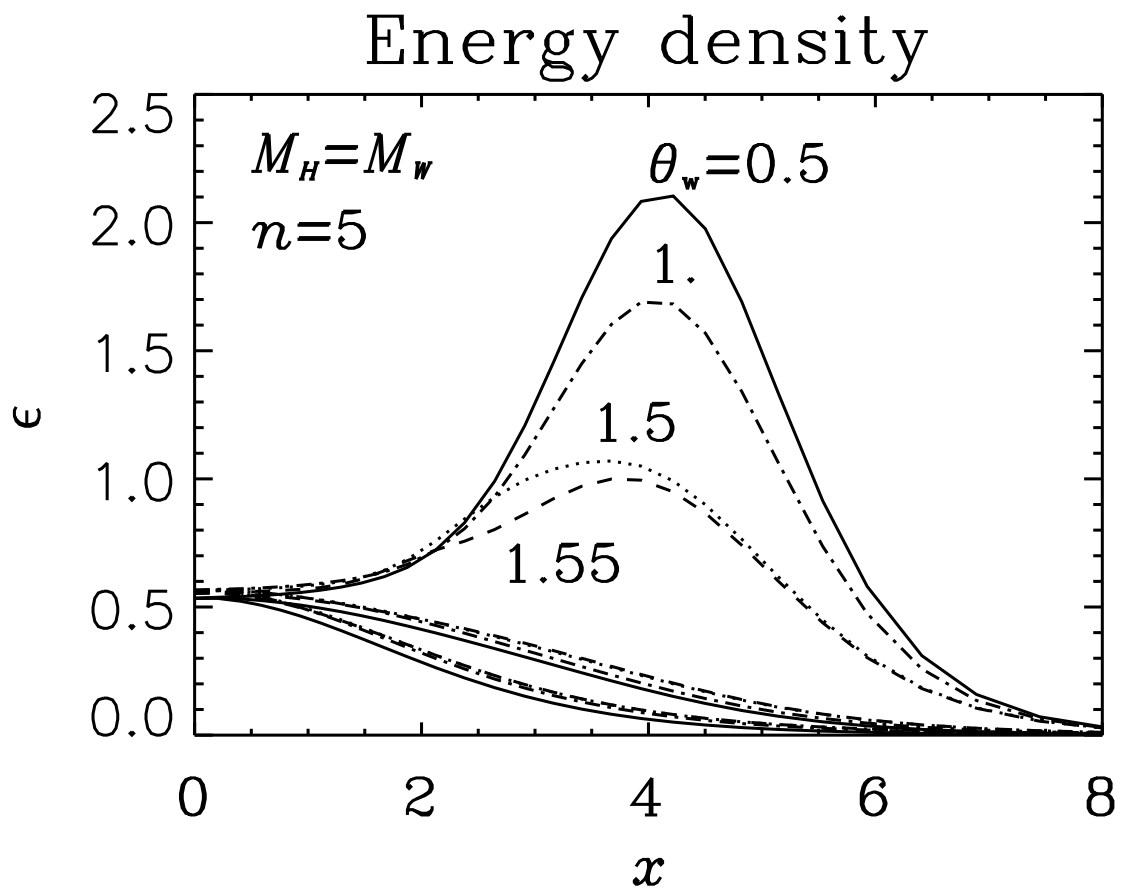


Figure 8b

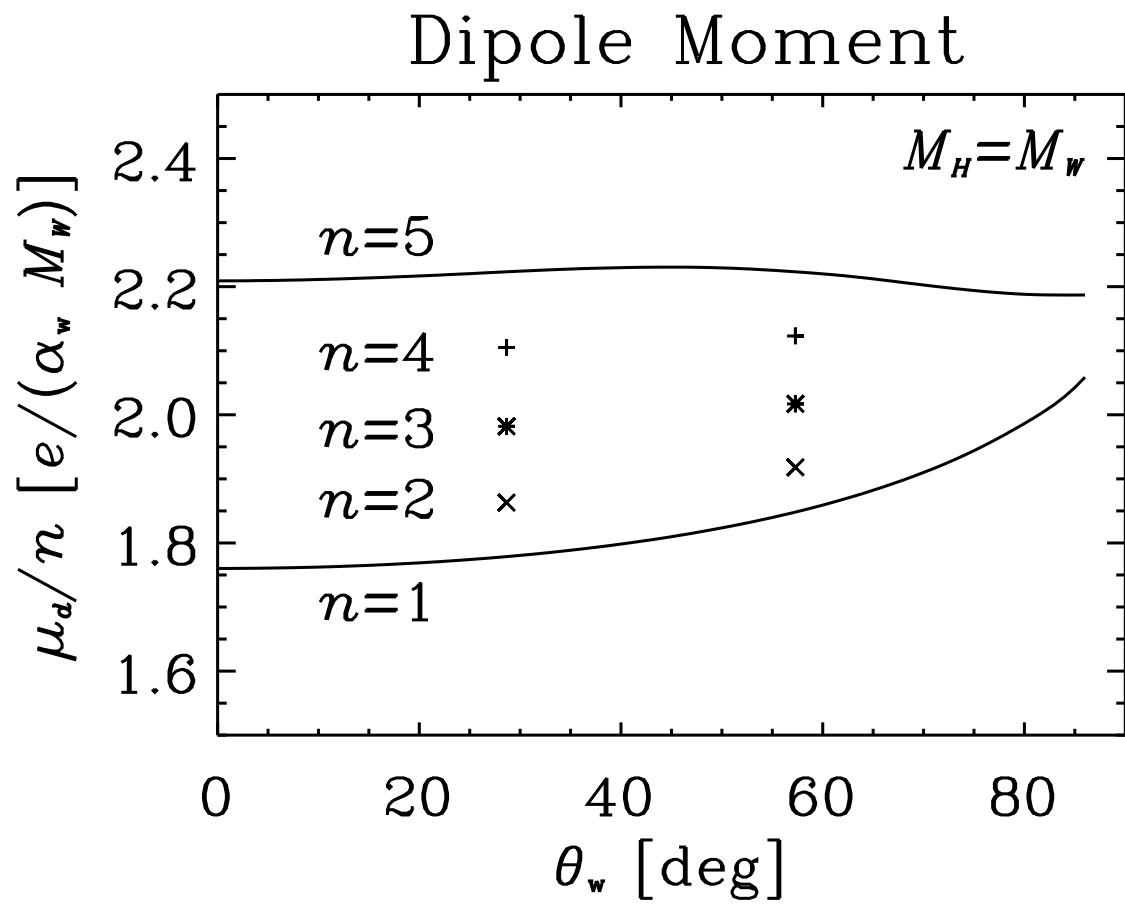


Figure 9